Communication

Super Typhoon Saola (2023) over the northern part of the South China Sea – aircraft data analysis

Junyi He , Pak Wai Chan * , Y.W. Chan , P. Cheung

Posted Date: 25 September 2023

doi: 10.20944/preprints202309.1683.v1

Keywords: tropical cyclone; aircraft data; turbulence; eddy dissipation rate

Communication

Super Typhoon Saola (2023) over the Northern Part of the South China Sea—Aircraft Data Analysis

Junyi He [1], P.W. Chan [2,*], Y.W. Chan [2] and P. Cheung [2]

[1] City University of Hong Kong, Hong Kong, China
[2] Hong Kong Observatory, Hong Kong, China

Abstract: In situ aircraft observations in typhoons have been scarce. This paper documents and analyses the aircraft and dropsonde data collected in Super Typhoon Saola (2023) over the northern part of the South China Sea. The wind and turbulence structures of the typhoon are investigated. The turbulence intensities are quantified in terms of turbulent kinetic energy (TKE) and eddy dissipate rate (EDR), and these data are compared with other available estimates of turbulence intensities, such as those based on weather radars, meteorological satellites, and numerical weather prediction (NWP) models. It is found that the TKE and EDR are closely correlated, and they are consistent with the weather radar/satellite observations as well as NWP-based outputs. Furthermore, the boundary layer inflow, vertical wind profiles, and atmospheric stability are analysed based on the dropsonde observations. The analysed results would advance the understanding of typhoon structures and offer references for the validation of remote sensing observations and NWP models.

Keywords: tropical cyclone; aircraft data; turbulence; eddy dissipation rate

Introduction

Tropical cyclones (TCs) produce among the strongest winds, surges, and economic losses of any atmospheric phenomenon. The basic understanding of TC structure and behaviour is essential to a number of practices, such as the track and intensity forecast of TCs in numerical weather prediction (NWP) models, TC-related wind, rainfall, and surge hazard prediction and early warning, and TC risk mitigation and loss reduction. This paper is the third one of the series of papers on super typhoon Saola in 2023. The first two ones are on meteorological observations from surface stations and ground-based remote sensing equipment, and on forecasting aspect respectively.

Since the introduction of TC research aircraft, e.g., National Oceanic and Atmospheric Administration (NOAA) WP-3D aircraft (Aberson et al.; 2006), along with GPS dropsondes (Hock & Franklin 1999; Wang et al., 2015), the understanding of TCs has significantly advanced. Various aspects of TC structure and behaviour have been investigated, e.g., wind structure (Kepert, 2006a, 2006b; Stern et al., 2016), boundary layer wind profiles (Franklin et al., 2003; Giammanco et al., 2013), momentum and heat fluxes (Powell et al., 2003; French et al., 2007; Drennan et al., 2007), turbulent kinetic energy (Zhang et al., 2011), dissipative heating (Zhang, 2010a), wind spectrum (Zhang, 2010b), and eddy diffusivity (Zhang & Montgomery, 2012; Zhang & Drennan, 2012; Zhao et al., 2019; Sparks et al., 2019; Gopalakrishnan et al., 2021). However, aircraft and dropsonde data are still far from enough for a comprehensive understanding of TCs. Specifically, aircraft observations in typhoons over the northwestern Pacific Ocean have been relatively scarce.

Since 2011, when there are TCs within the Hong Kong Flight Information Region (HKFIR) over the northern part of the South China Sea, the Hong Kong Observatory (HKO) would collaborate with Government Flying Service (GFS) to conduct TC reconnaissance flight (Hon and Chan, 2022). Before that, measurements were made on an ad hoc basis, e.g. during search and rescue exercise within typhoons (e.g. Chan et al., 2011). At first, only in situ measurements were available using a 5-hole probe, recording the three components of the wind, pressure, temperature and humidity (Chan et al.,

 doi:10.20944/preprints202309.1683.v1

2014). Later on, dropsonde capability has been made available, and now both probe and dropsonde data are collected (Chan et al., 2018).

Super Typhoon Saola in August to September 2023 had significant impacts on the weather along the south China coast. Two TC reconnaissance flights had been conducted for Saola, namely, on 31 August and 1 September 2023. Probe and dropsonde data were available in the first flight. For the second flight when Saola was very close to Hong Kong, unfortunately only probe data were available, but photos had been taken by the pilots on the typhoon eye.

This paper documents the measurements made during the two flights. Analysis of the data has been made, especially on the turbulence intensities in terms of turbulent kinetic energy (TKE) and eddy dissipate rate (EDR), and these data are compared with other available estimates of turbulence intensities such as based weather radars and meteorological satellites, as well as from numerical weather prediction (NWP) models. Dropsonde data have also been analyzed.

This is the first time that in situ aircraft and dropsonde data are collected in and above the eyewall of a Super Typhoon over this ocean basin. The data collected and analyzed are useful for enhancing the understanding of TC structure and behaviour and for validating remote sensing observations and NWP models.

Analysis of flight data

The flight data was collected by the Aircraft Integrated Meteorological Measuring System 20 Hz (AIMMS20) installed on the Bae Jetstream 4100 (J41) fixed-wing aircraft of GFS. The system measures three orthogonal components of wind velocity, temperature, relative humidity, and pressure at a frequency of 20 Hz. A detailed description of the AIMMS20 can be found in Beswick et al. (2008), and the system setup is reported in Chan et al. (2011).

The two flights were conducted between around 07 and 09 UTC, 31 August 2023, and between around 01 and 02 UTC, 1 September 2023, respectively. Figure 1 shows some selected horizontal wind data along the flights. It could be seen that both flights had been conducted rather close to the eye of Saola at the respective time. The winds were the strongest when the aircraft was located close to the eyewall of Saola, reaching hurricane force wind (wind barbs coloured orange in Figure 1) whilst the aircraft reached a height of around 10 km above the sea surface.

In the flight of 1 September, the aircraft had penetrated through the eye of Saola, as shown in Figure 1b. At that time the pilots had taken some pictures about the typhoon eyes and the associated clouds, as shown in Figure 2. The eye of Saola shows up clearly in these pictures. This is the first time that the eye of a super typhoon had ever been visited by an aircraft over the South China Sea, according to the knowledge of the authors and the news.

The time series of the horizontal wind speed and direction as well as the vertical component of the wind during the two flights are shown in Figures 3 and 4 respectively. For the first flight (Figure 3), the maximum measured wind speed was around 36 m/s, and was captured for one time only. The vertical component of the wind was mostly positive, i.e. upward motion. For the second flight (Figure 4), maximum winds of around 40 m/s had been captured for a couple of times, with lower wind speed in between. The horizontal wind direction also went through a full circulation as the aircraft got inside and around the typhoon eye. In the eye region, there are both strong upward and downward motions. Positive vertical velocity (upward motion) reaches about 10 m/s, and negative vertical velocity (downward motion) reaches about −7 m/s. Within the eye when the horizontal wind direction went through a circle, the vertical velocity changed from rather positive (generally 5 m/s or above) to not so positive/even negative (generally below 5 m/s).

The air temperature, air pressure and relative humidity of the two flights are shown in Figures 5 and 6 respectively. The corresponding altitudes are given in Figure 7. The temperature and humidity do not show very interesting features. For the relative humidity (Figure 5c), as the aircraft was mostly inside clouds in the first flight, it remained relatively high throughout the flight. On the other hand, the aircraft flew around the eye of Saola in the second flight, so that the relative humidity (Figure 6c) shows significant fluctuations, and it could reach around 30% in the relatively clear region within the eye.

Preprints (www.preprints.org) | NOT PEER-REVIEWED | Posted: 25 September 2023 doi:10.20944/preprints202309.1683.v1

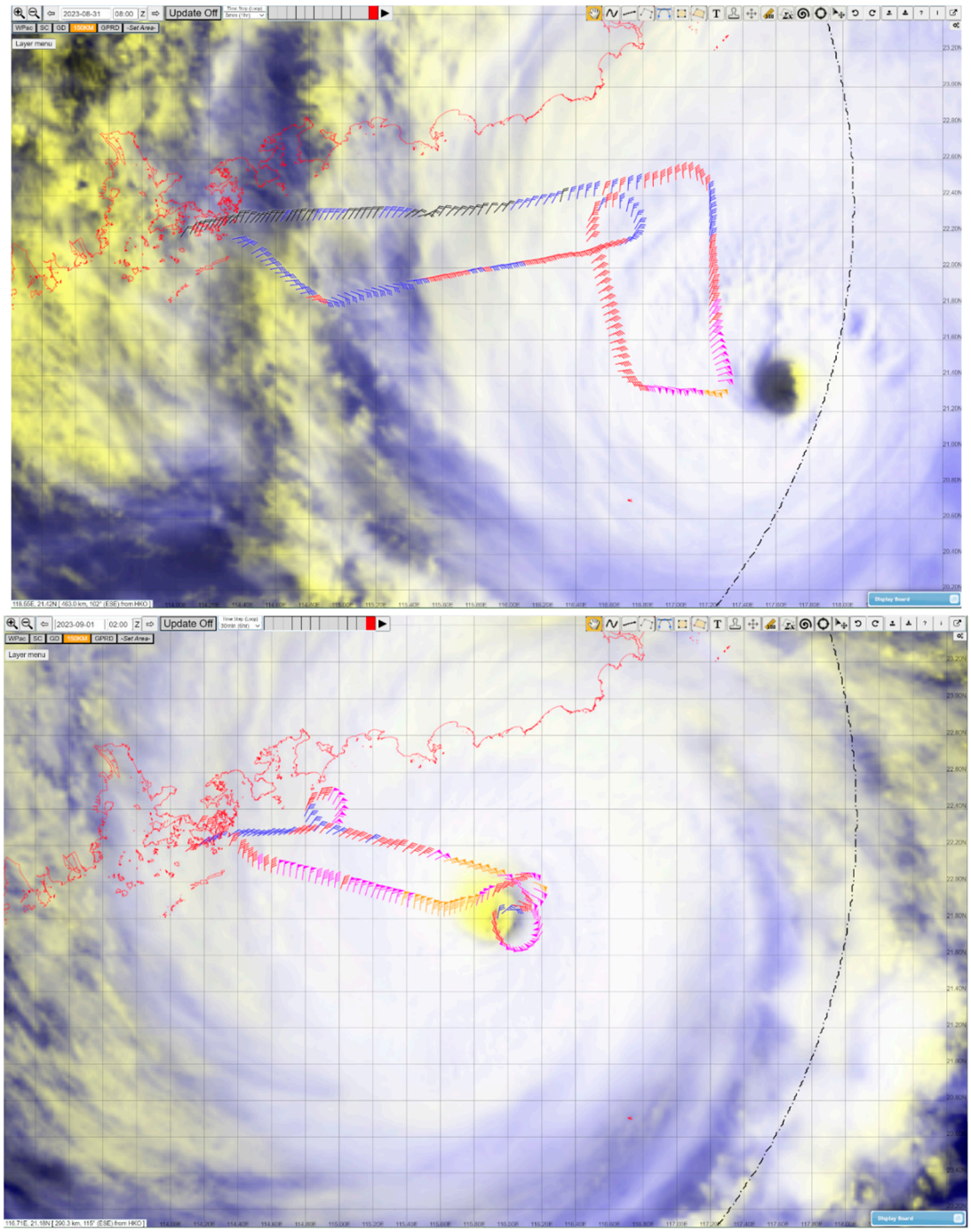

Figure 1. Flight routes and horizontal wind data along the flights. Upper panel: flight between around 07 and 09 UTC, 31 August 2023; lower panel: flight between around 01 and 02 UTC, 1 September 2023.

 doi:10.20944/preprints202309.1683.v1

Figure 2. Photos about the typhoon eyes and the associated clouds taken during the eyewall penetration on 1 September 2023.

Preprints (www.preprints.org) | NOT PEER-REVIEWED | Posted: 25 September 2023 doi:10.20944/preprints202309.1683.v1

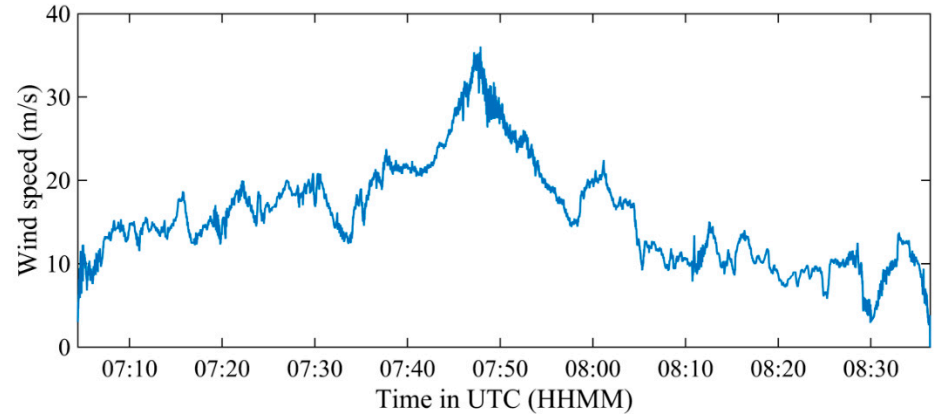

(a)

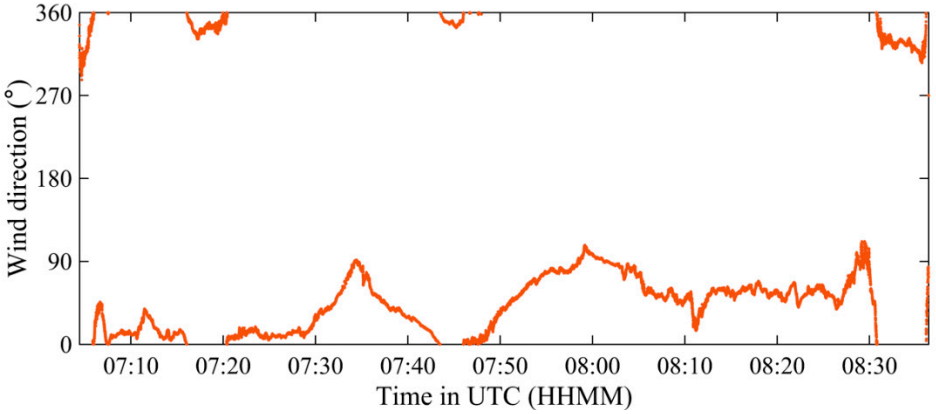

(b)

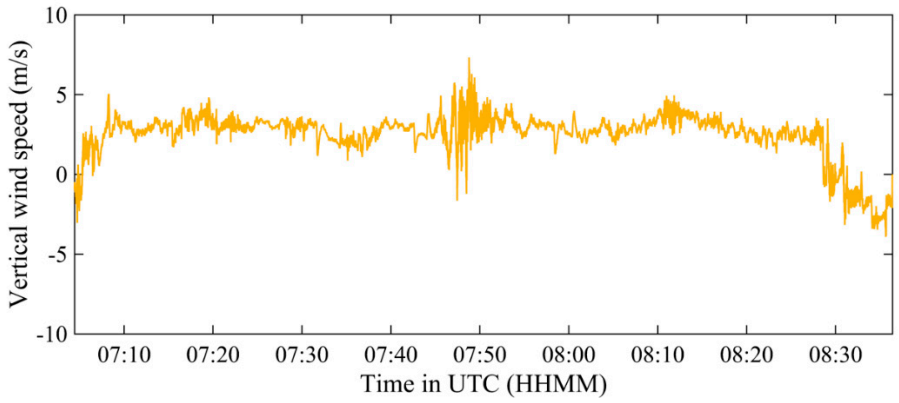

(c)

Figure 3. Time series of the (a) horizontal wind speed, (b) wind direction, and (c) vertical wind speed based on the aircraft data on 31 August 2023.

Preprints (www.preprints.org) | NOT PEER-REVIEWED | Posted: 25 September 2023 doi:10.20944/preprints202309.1683.v1

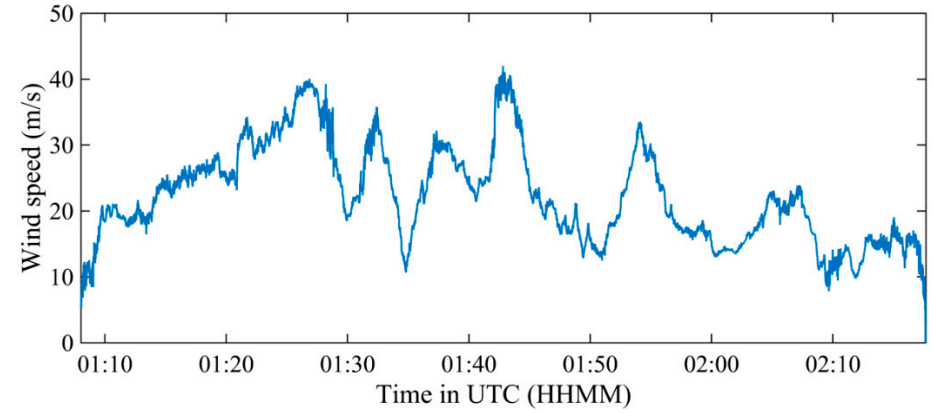

(a)

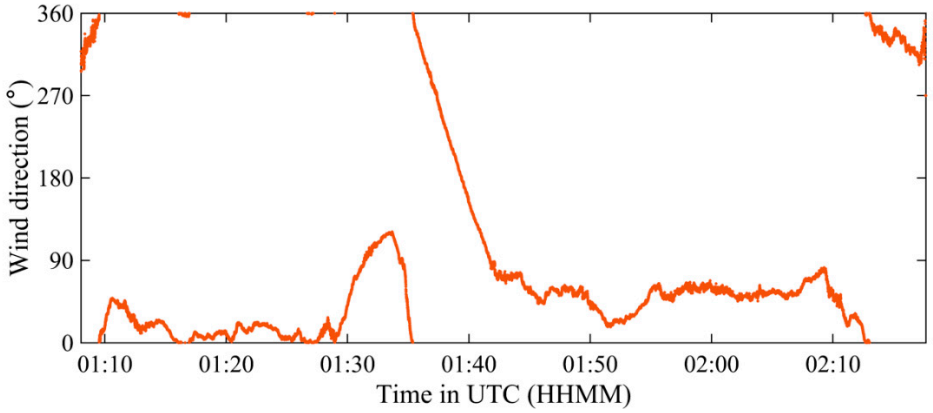

(b)

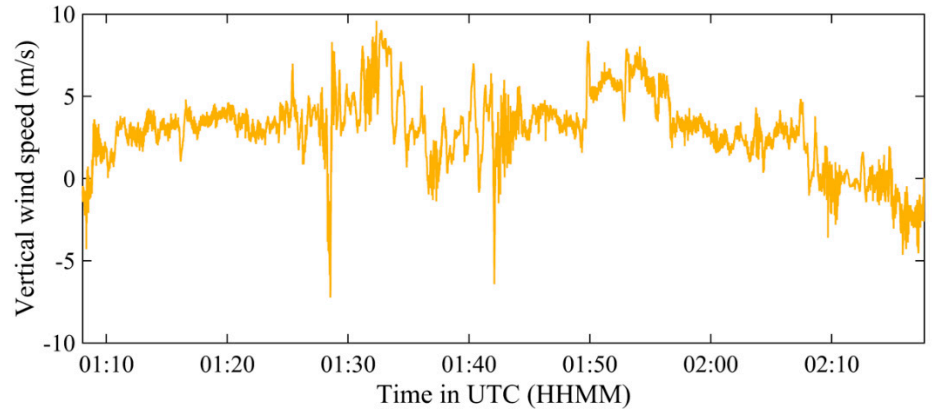

(c)

Figure 4. As in Figure 3, but for 1 September 2023.

Preprints (www.preprints.org) | NOT PEER-REVIEWED | Posted: 25 September 2023 doi:10.20944/preprints202309.1683.v1

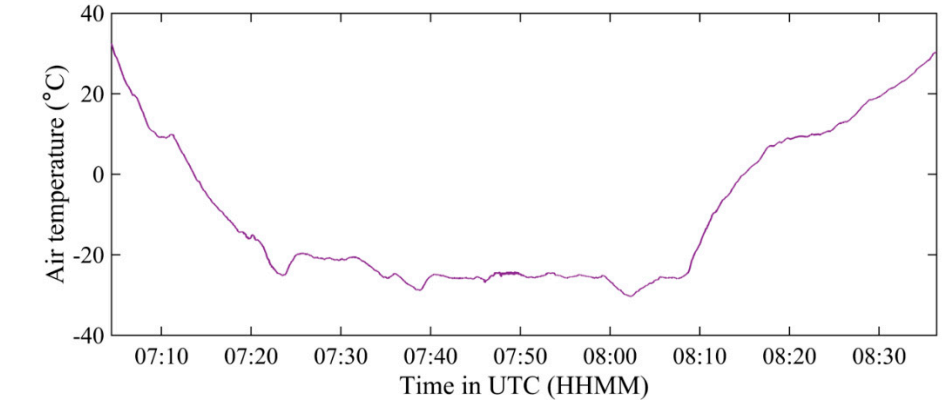

(a)

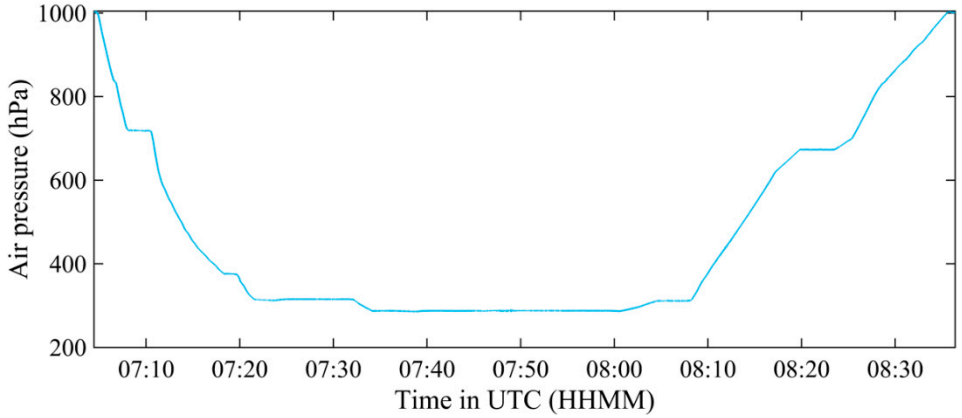

(b)

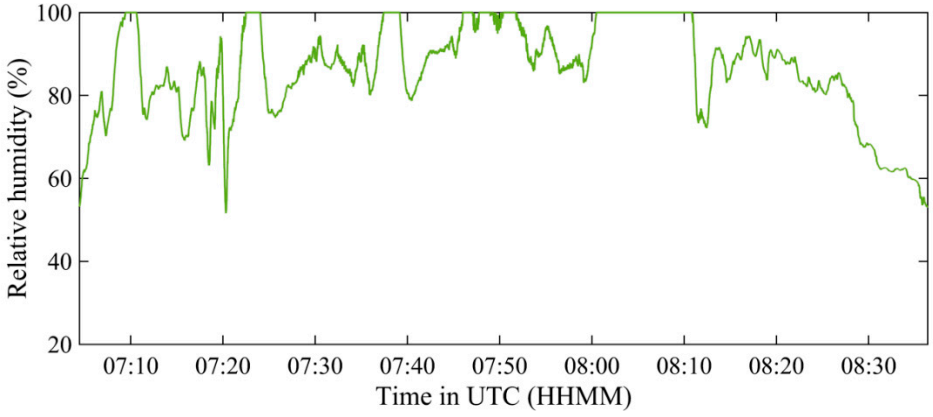

(c)

Figure 5. Time series of the (a) temperature, (b) pressure, and (c) relative humidity based on the aircraft data on 31 August 2023.

Preprints (www.preprints.org) | NOT PEER-REVIEWED | Posted: 25 September 2023 doi:10.20944/preprints202309.1683.v1

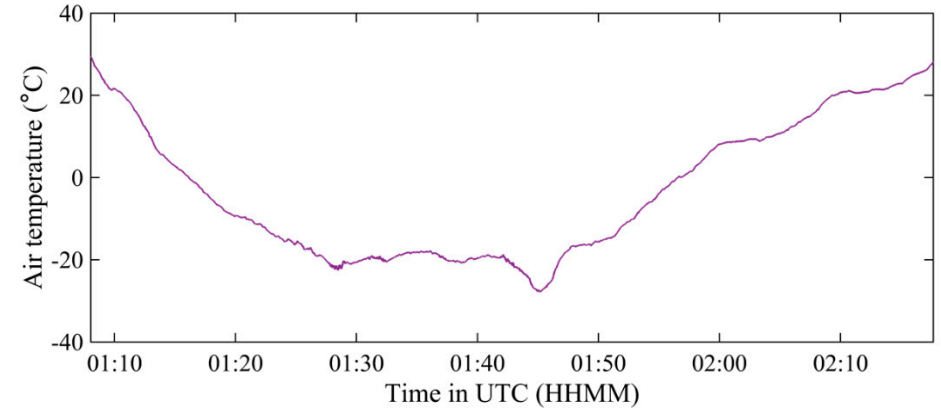

(a)

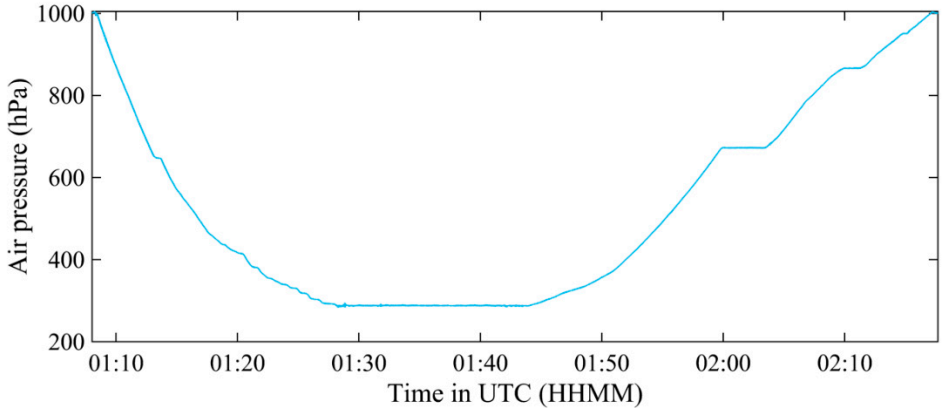

(b)

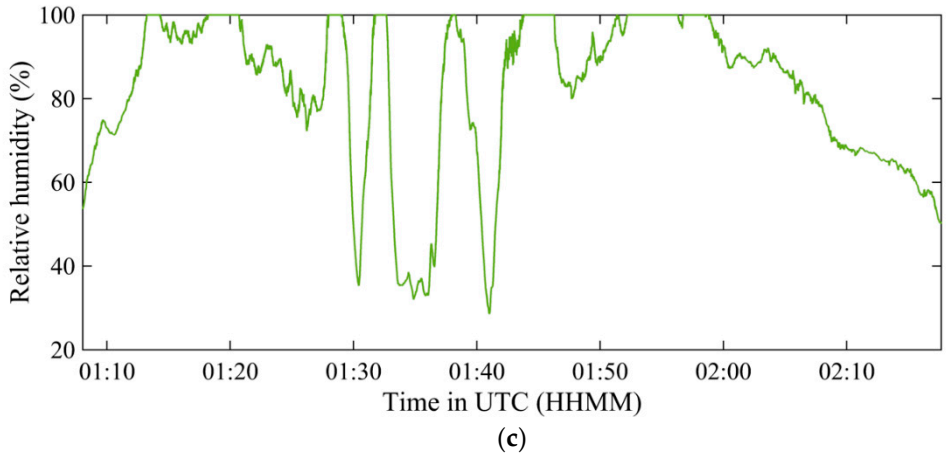

(c)

Figure 6. As in Figure 5, but for 1 September 2023.

Preprints (www.preprints.org) | NOT PEER-REVIEWED | Posted: 25 September 2023 doi:10.20944/preprints202309.1683.v1

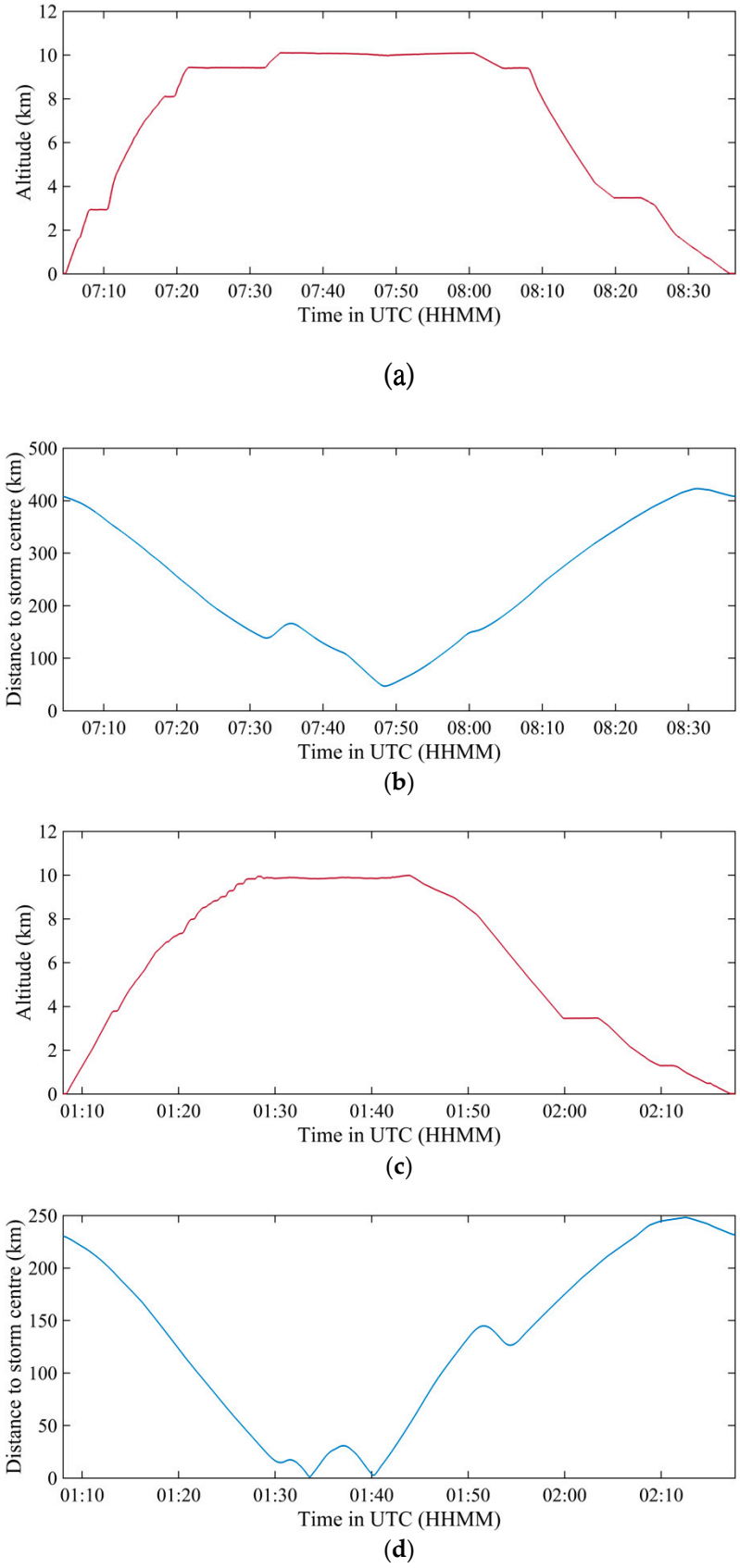

Figure 7. Time series of the flight altitude and distance to storm centre on (a)(b) 31 August 2023 and (c)(d) 1 September 2023.

Preprints (www.preprints.org) | NOT PEER-REVIEWED | Posted: 25 September 2023 doi:10.20944/preprints202309.1683.v1

Eddy dissipation rate and turbulent kinetic energy

The estimation of turbulent kinetic energy (TKE) and eddy dissipation rate (EDR, ε) follows the procedures described in Zhang et al. (2011), Sparks et al. (2019), etc. Turbulent fluctuations are extracted by detrending the three orthogonal components of wind velocity in a least-squares manner. A high-pass filter with a cut-off frequency of 0.01 Hz was employed before the detrending. Based on the turbulent fluctuations, the TKE (per unit mass) is calculated as:

$$TKE = \frac{1}{2}(\sigma_u^2 + \sigma_v^2 + \sigma_w^2) \quad (1)$$

where σu, σv, and σw are the standard deviations of along-wind, cross-wind, and vertical wind velocity components. Following Zhang et al. (2011) and Sparks et al. (2019), the EDR can be estimated based on the power spectral density of along-wind velocity component in the inertial subrange:

$$\varepsilon = {\alpha_u}^{-3/2} \frac{2\pi n}{U_a} [nS_u(n)]^{3/2} \quad (2)$$

where αu is the Kolmogorov constant for along-wind velocity component taken as 0.5 (Sreenivasan, 1995), Ua is the true air speed, and Su(n) is the along-wind velocity spectrum at frequency n, which should be located within the inertial subrange. Generally, for the flight data analyzed here, the inertial subrange with a slope close to −5/3 covers 0.4–4 Hz, therefore the EDR is estimated based on the wind spectrum over this frequency range.

The TKE and EDR are shown in Figures 8 and 9 respectively for the two flights. For the first flight (Figure 8), there was a single peak with EDR reaching about 0.3 when the aircraft was close to the typhoon eye. For the second eye (Figure 9), the EDR was generally higher when the aircraft was located at the eyewall or within the eye. It was generally in the order of 0.1 to 0.3.

The local closure techniques are widely used for turbulence parameterization in numerical weather models (Mellor and Yamada, 1974). For a local 1.5-order closure, ε can be parameterized as a function of TKE1.5 (Stull, 1988), or equivalently, there is a relationship between ln(ε) and ln(TKE) with a slope of 1.5. Such a relationship is also widely reported in observational studies, e.g., in Vecenaj et al. (2010). Chan et al. (2011), based on aircraft observations in TCs, also showed the slope between ln(ε) and ln(TKE) is close to 1.5. The TKE and EDR from the two flights have been plotted together in scattered plots, and the results are shown in Figures 8c and 9c. In general, they show good correlations, and the best fit straight lines are shown in these figures. For the 31 August and 1 September cases, the linear regression slopes between ln(ε) and ln(TKE) are 1.75 and 1.51, respectively, which are close to the predicted slope of 1.5 by the local 1.5-order closure parameterization and agree with the previous observations.

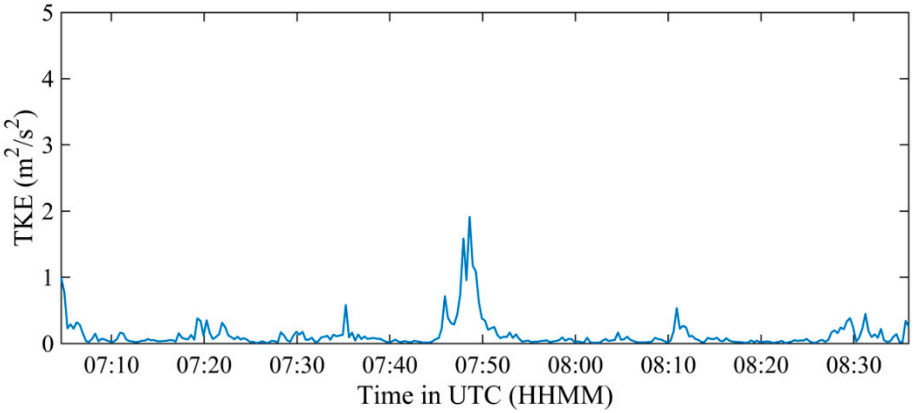

(a)

Preprints (www.preprints.org) | NOT PEER-REVIEWED | Posted: 25 September 2023 doi:10.20944/preprints202309.1683.v1

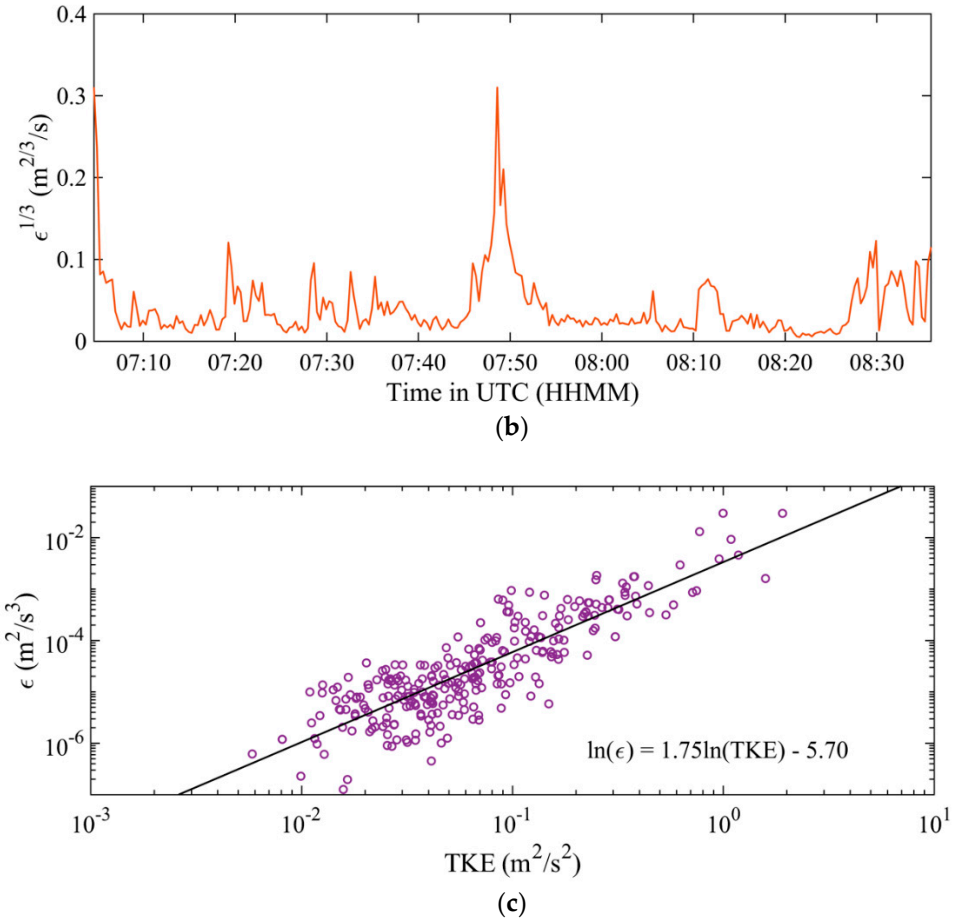

Figure 8. (a) Time series of the turbulent kinetic energy (TKE) based on the aircraft data on 31 August 2023, (b) time series of the cube root of the eddy dissipation rate (ε1/3), and (c) variation of ε with TKE. The black line in c represents the linear fit between ln(ε) and ln(TKE).

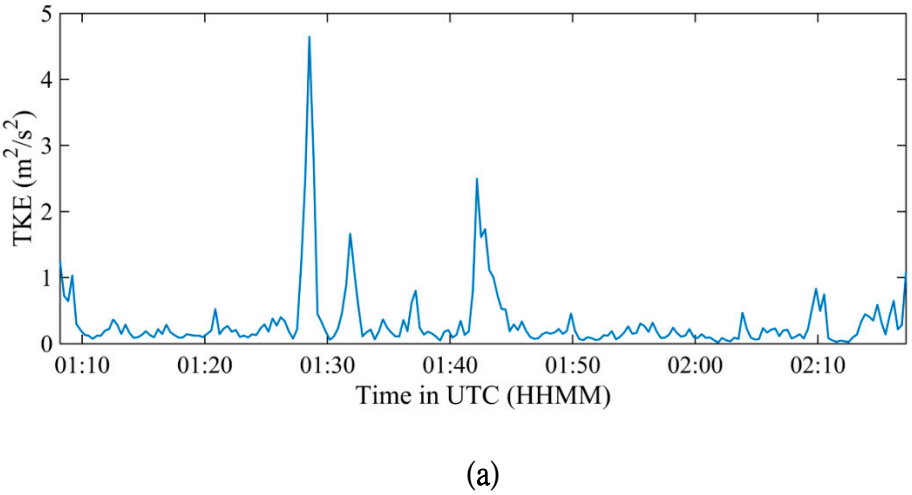

Preprints (www.preprints.org) | NOT PEER-REVIEWED | Posted: 25 September 2023 doi:10.20944/preprints202309.1683.v1

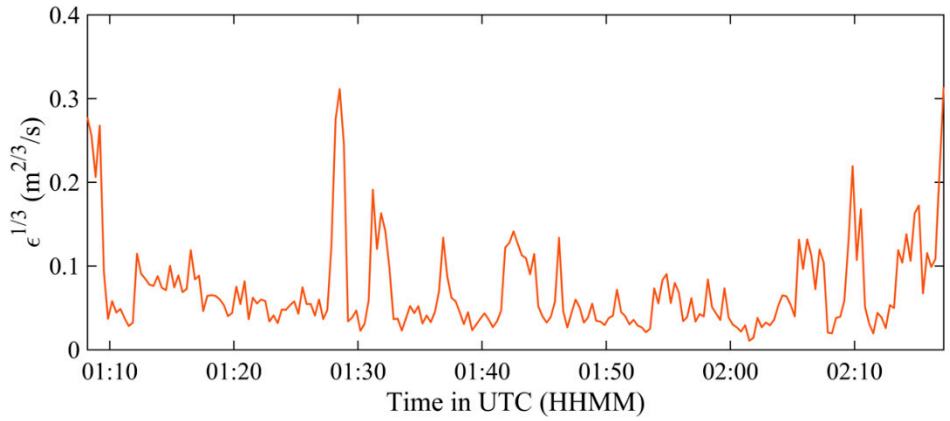

(**b**)

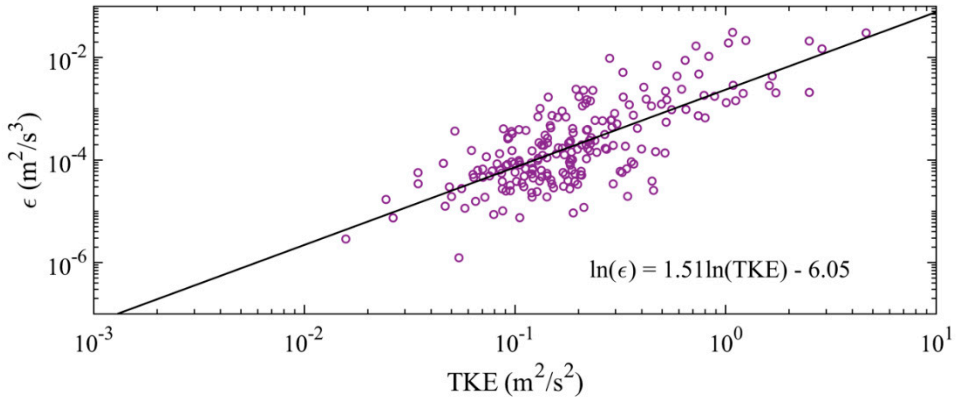

(**c**)

Figure 9. As in Figure 8, but for 1 September 2023.

EDR comparison with radar, satellite and model data

EDR has been estimated from the spectral widths of the weather radars over southern China, based on the methods described in Chan et al. (2016). Such data are only available when Saola was close to the weather radars, and so the results at the time of the second flight are shown in Figure 10. Only EDR data at 1, 2, 3 and 4 km above sea level are available. Figure 10 shows the results of 4 km height. At that time, the aircraft recorded EDR at around 0.1, which is consistent with the estimation from the radar. This is the first time that the weather radar based EDR could be verified using aircraft data in a typhoon situation.

An estimate of the turbulence intensity could also be made based on the gravity waves as captured by water vapour channel of the geostationary meteorological satellites. Some background information of the methodology could be found in Wimmers et al. (2018). Such turbulence intensities are available in real time in HKO and their spatial distributions around Saola at about the times of the two flights are shown in Figure 11. Gravity waves clearly show up from the analysis of the water vapour satellite pictures. The turbulence intensity is estimated to be of class “moderate”, which is coloured yellow in Figure 11. This result is consistent with the EDR measurements of 0.3 from the aircraft data.

Turbulence intensity is also estimated from NWP models. HKO uses the method as suggested in Kwok et al. (2022) and the NWP-based turbulence maps are generated in real time. Examples of the maps at the times of the two flights are shown in Figure 12. Again, moderate turbulence is estimated at the pressure level of 300 hPa, which is around the height of the aircraft when it was close to the typhoon eyes. Again, the NWP-based estimates are consistent with the actual observations from the aircraft.

Preprints (www.preprints.org) | NOT PEER-REVIEWED | Posted: 25 September 2023 doi:10.20944/preprints202309.1683.v1

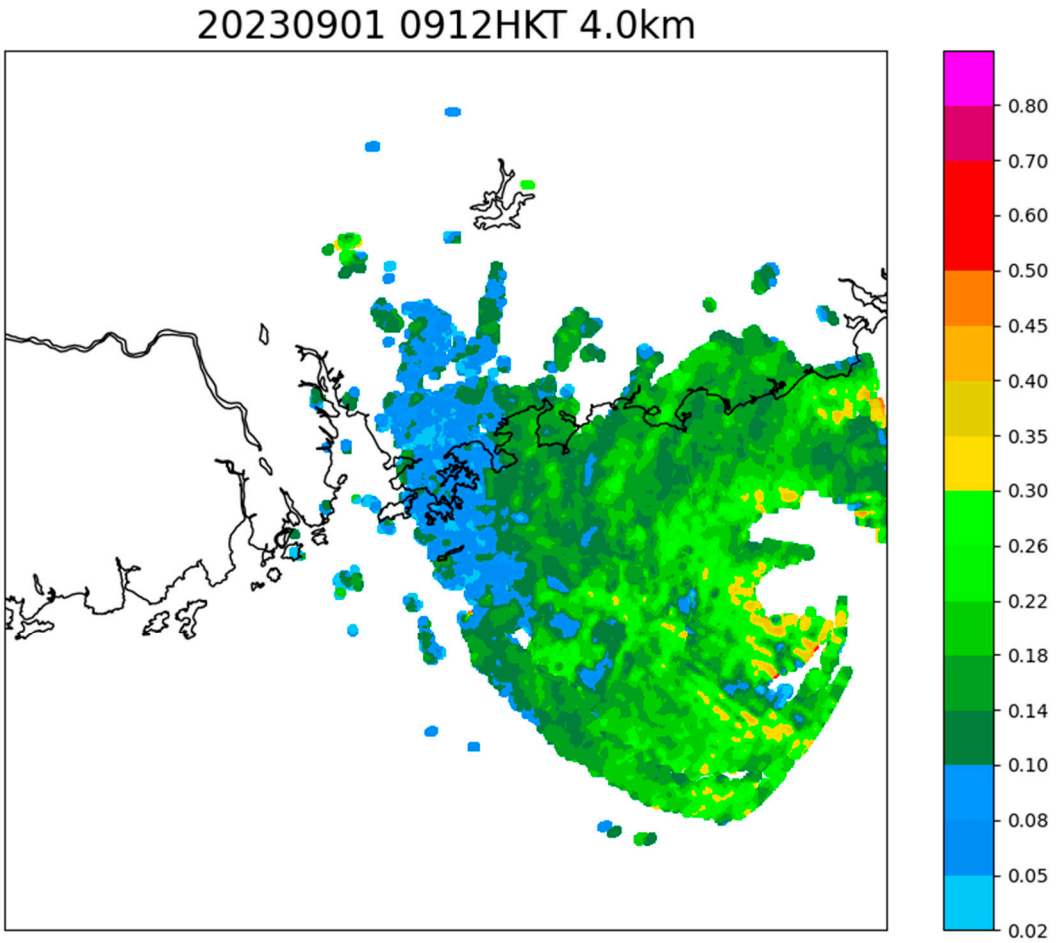

Figure 10. estimated from the spectral widths of the weather radars.

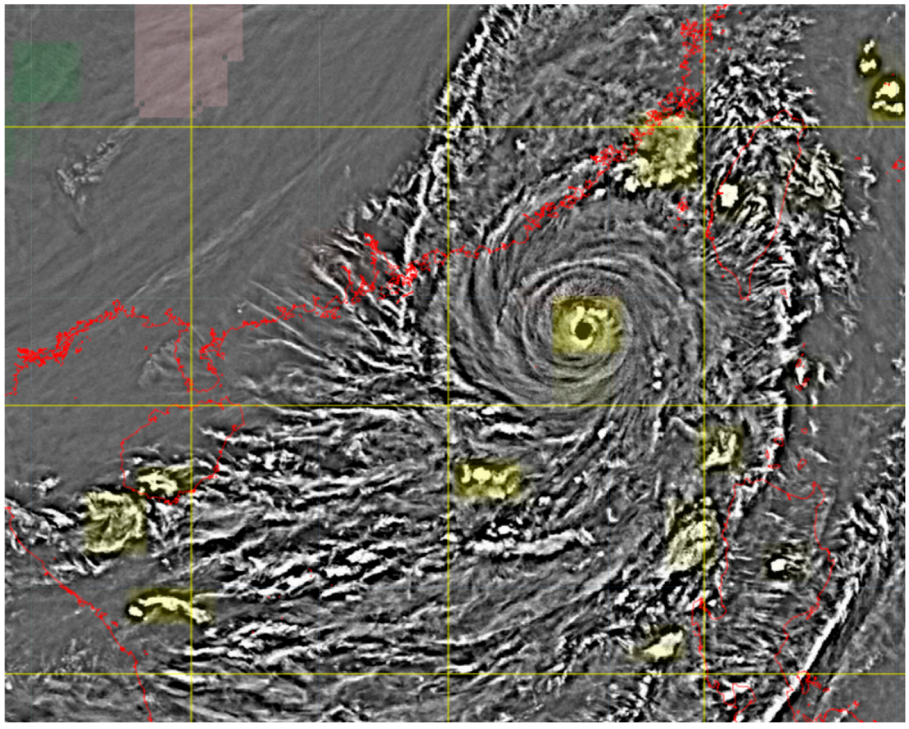

07:50 UTC on 31 August 2023

Preprints (www.preprints.org) | NOT PEER-REVIEWED | Posted: 25 September 2023 doi:10.20944/preprints202309.1683.v1

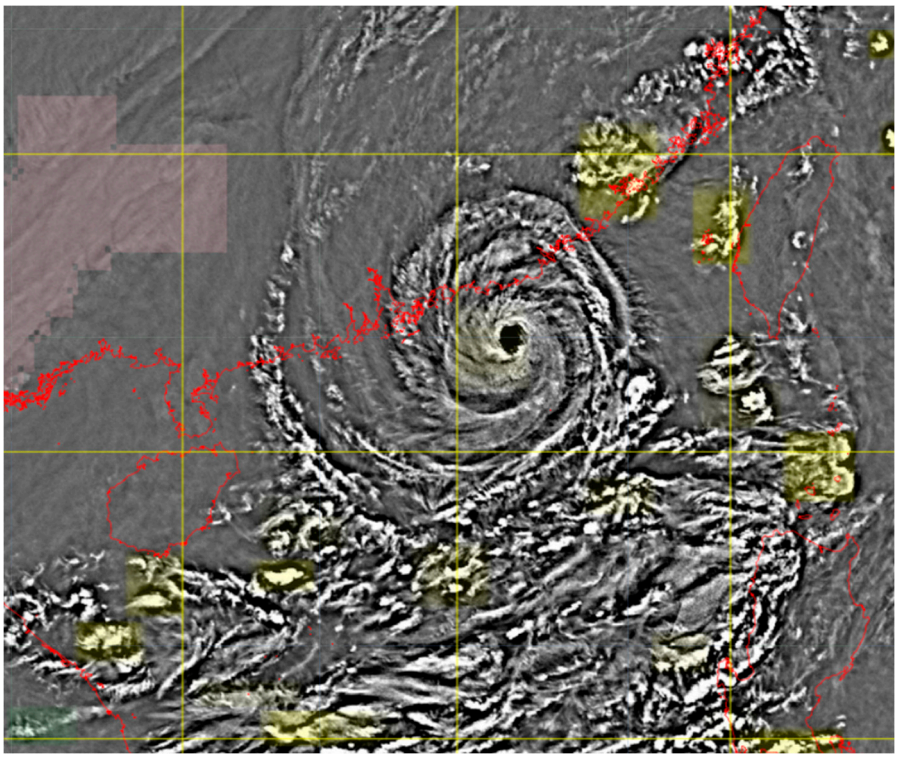

01:30 UTC on 1 September 2023

Figure 11. Gravity waves as captured by water vapour channel of the geostationary meteorological satellites. The turbulence intensity estimated to be of class "moderate" is coloured yellow.

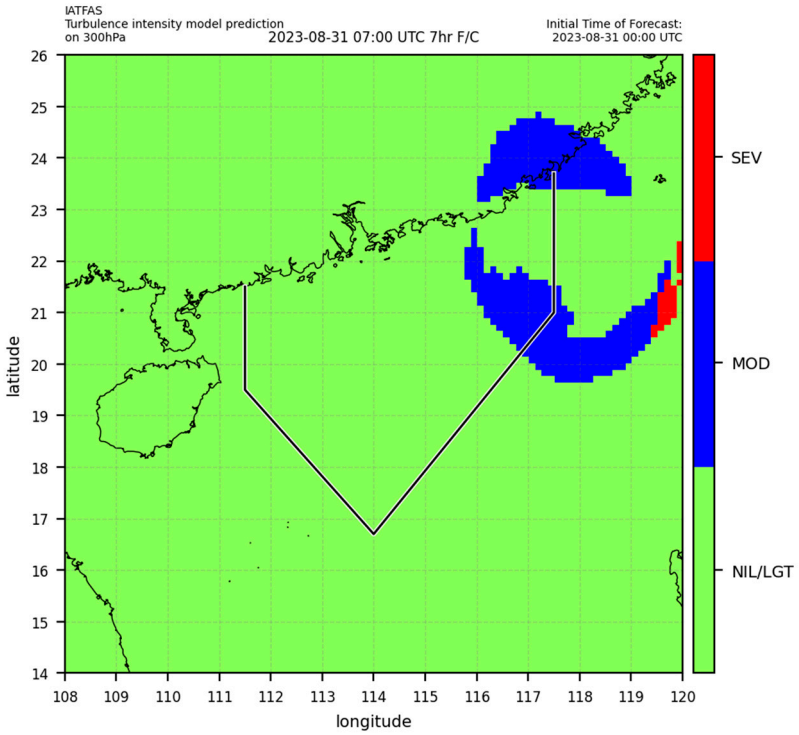

Preprints (www.preprints.org) | NOT PEER-REVIEWED | Posted: 25 September 2023 doi:10.20944/preprints202309.1683.v1

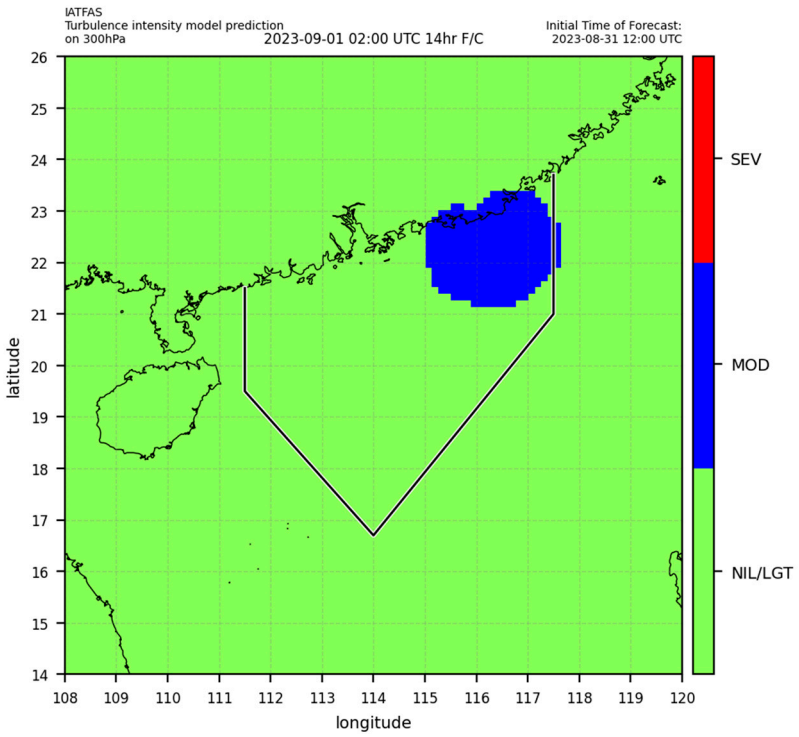

Figure 12. Turbulence intensity estimated from the NWP model.

Dropsonde observation

Dropsondes were deployed by the aircraft at an altitude of 10 km. During their descent from 10 km to the sea surface, they collect continuous measurements of vertical profiles of wind speed and direction at a frequency of 4 Hz, along with temperature, humidity, and pressure at a frequency of 2 Hz. Typically, a dropsonde completes its descent in less than 15 minutes. An overview of the GPS dropsonde dataset can be found in Wang et al. (2015), and a detailed description of the dropsonde measurements by the HKO can be found in, e.g., Chan et al. (2018) and He et al. (2022a). The dropsonde data were quality controlled using the ASPEN software with Editsonde configuration following Zhang et al. (2013) and Stern et al. (2015).

Dropsonde data are available in the first flight only. The vertical profiles of inflow and equivalent potential temperatures are shown in Figures 13 and 14 respectively. It could be seen that the atmospheric boundary layer, i.e. below around 1 km, was mostly inflow from the sondes. The heights of the maximum wind speed are also generally around 1 km, which is close to or slightly lower than the inflow layer height. This is consistent with the previous observations of TC boundary layer height scales (Zhang et al., 2011). The equivalent potential temperature profiles also showed unstable boundary layer. As such, Saola remained to be a rather strong system as it moved towards the south China coast. This is consistent with the results, e.g. in He et al. (2022b).

The vertical wind profiles in the boundary layer of the TC, i.e., the first 1 km or so above the sea level, are shown in Figure 15. For the sonde that is closest to the typhoon eye, wind speed as high as 40 m/s had been recorded. Various wind profile models, including the logarithmic law, the Vickery et al. (2009) model, the Gryning et al. (2007) model, the Deaves & Harris (1978) model, and the power law, were used to fit the observed wind profiles in a least-squares manner. In general, the Vickery model gives the best fit to the vertical wind profiles. This agrees with previous observations (e.g., Chan et al., 2023; He et al., 2023) and indicates that the simple power law, which is extensively used in building design codes (e.g., ASCE7) and wind turbine standards (e.g., IEC61400) for wind load estimation, may not be applicable to TC environments.

Preprints (www.preprints.org) | NOT PEER-REVIEWED | Posted: 25 September 2023 doi:10.20944/preprints202309.1683.v1

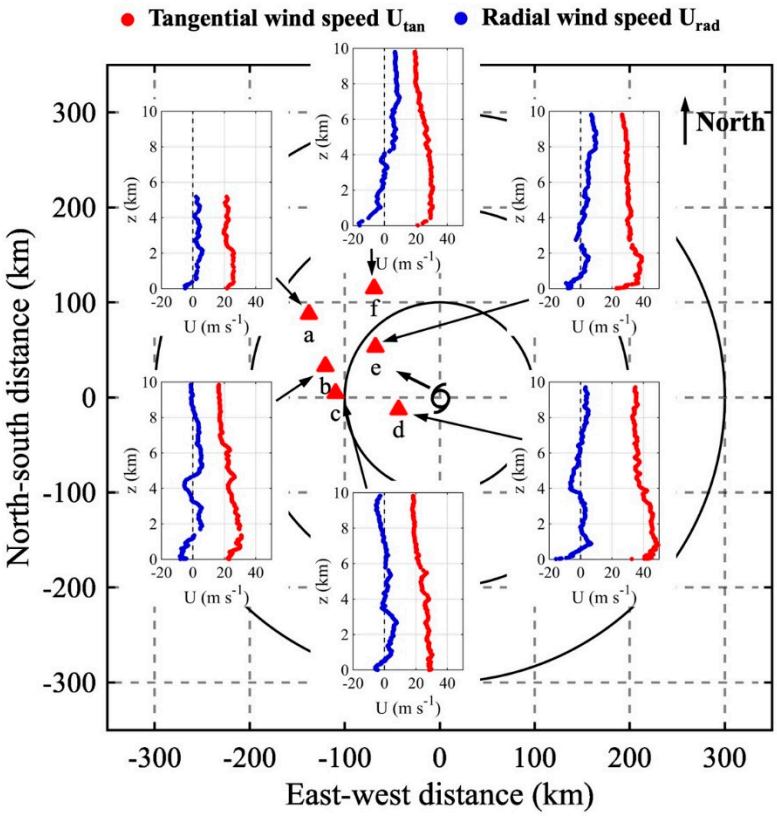

Figure 13. Vertical profiles of tangential (red) and radial (blue) wind speeds in Typhoon Saola at around 0800UTC 31 August 2023. Tangential wind speed: anti-clockwise positive; radial wind speed: outflow positive. Red triangles represent dropsonde locations relative to the storm center.

Preprints (www.preprints.org) | NOT PEER-REVIEWED | Posted: 25 September 2023 doi:10.20944/preprints202309.1683.v1

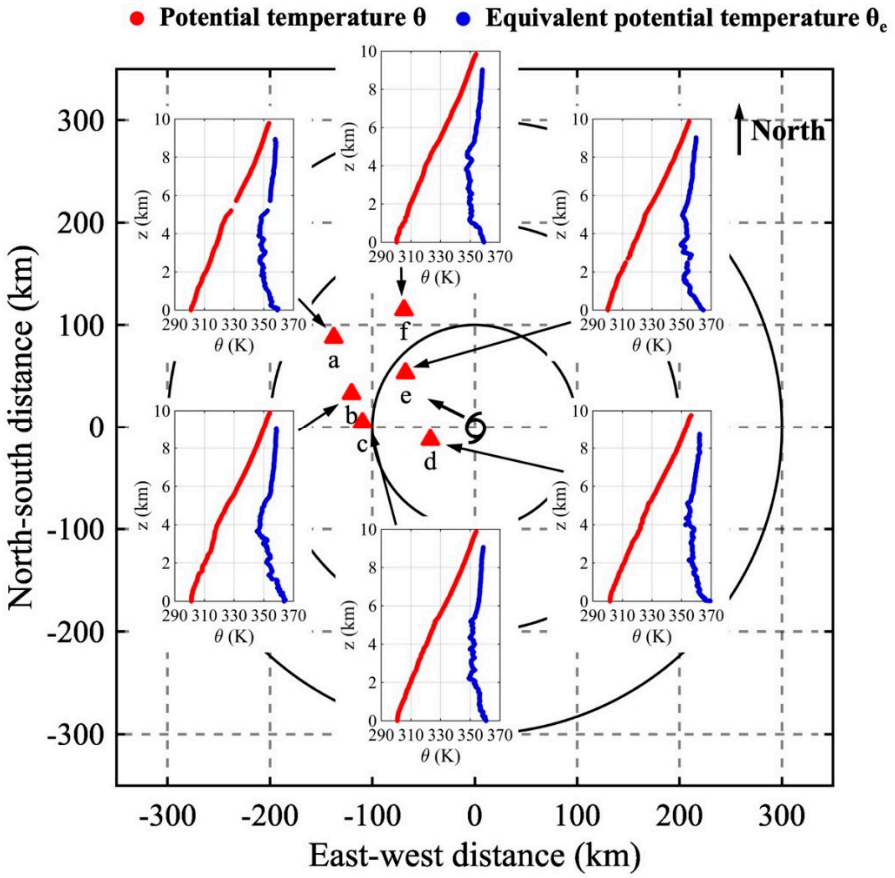

Figure 14. Vertical profiles of potential temperature (red) and equivalent potential temperature (blue) in Typhoon Saola at around 0800UTC 31 August 2023. Red triangles represent dropsonde locations relative to the storm center.

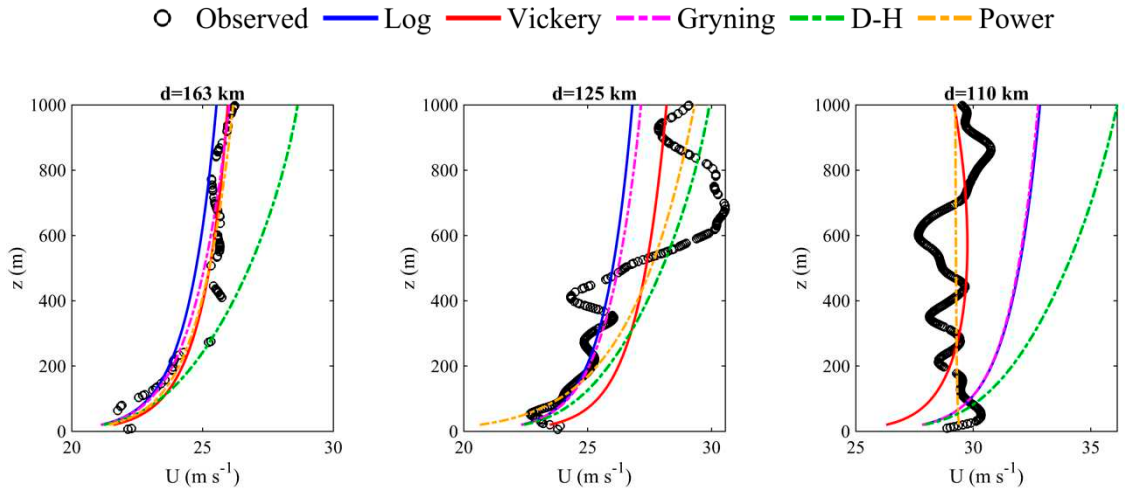

Preprints (www.preprints.org) | NOT PEER-REVIEWED | Posted: 25 September 2023 doi:10.20944/preprints202309.1683.v1

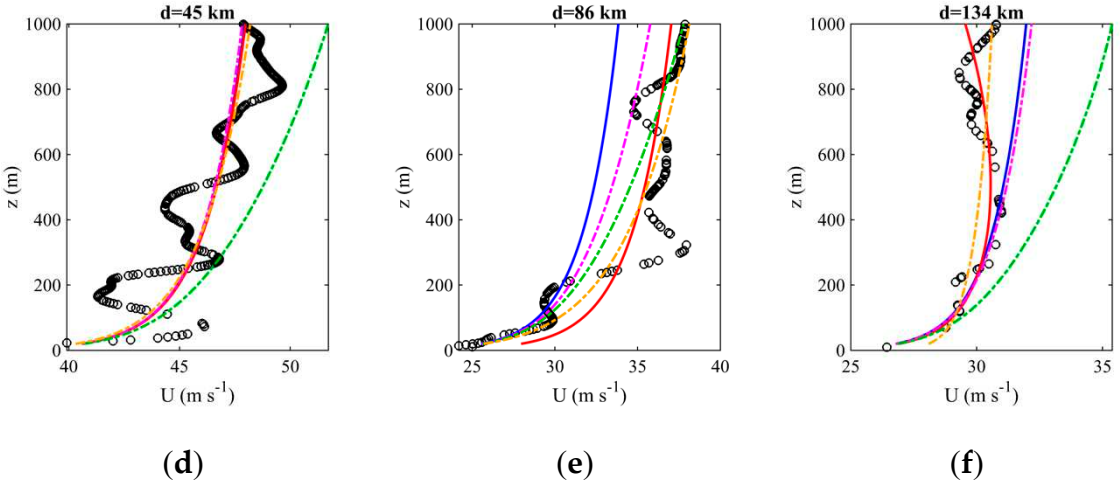

Figure 15. Fitting of vertical profiles of wind speeds in the lowest 1000 m in Typhoon Saola to the wind profile models, including the logarithmic law, Vickery et al. (2009) model, Gryning et al. (2007) model, Deaves & Harris (1978) model, and power law. d represents the distance to the storm center.

Conclusions

TC reconnaissance flights had been conducted for Super Typhoon Saola over the northern part of the South China Sea. The flight data provided some insights into the structure of the TC. The general structure of the TC, e.g., maximum wind speed of up to 40 m/s near the eyewall and low wind speed within the eye, low relative humidity within the eye, near-surface inflow in the lowest 1 km, and unstable boundary layer, were captured by the aircraft and dropsonde observations. Updrafts of up to 10 m/s and downdrafts of up to 7 m/s were observed near the eyewall.

Turbulence was also measured during the flights. In particular, EDR and TKE data are available. There is stronger turbulence in terms of TKE and EDR in/near the eyewall of the TC than the other parts. This is consistent with previous observations. The EDR is generally proportional to the TKE raised to the power of approximately 1.5, which agrees with the 1.5-order turbulence parameterization. The values of EDR from in situ aircraft observations are consistent with the other observations/NWP-based outputs. This is a new finding for super typhoons in the region.

More aircraft data would be collected in the future. And a database of typhoon observations, particularly for the winds, would be built up for this part of the world. The turbulence intensity would be a major subject for the study.

References

1. Aberson, S. D., Black, M. L., Black, R. A., Burpee, R. W., Cione, J. J., Landsea, C. W., & Marks Jr., F. D. (2006). Thirty years of tropical cyclone research with the NOAA P-3 aircraft. Bulletin of the American Meteorological Society, 87, 1039-1055.
2. Beswick, K. M., Gallagher, M. W., Webb, A. R., Norton, E. G., & Perry, F. (2008). Application of the Aventech AIMMS20AQ airborne probe for turbulence measurements during the Convective Storm Initiation Project. Atmospheric Chemistry and Physics, 8, 5449-5463.
3. Chan, P. W., Choy, C. W., Mak, B., & He, J. Y. (2023). A rare tropical cyclone necessitating the issuance of gale or storm wind warning signal in Hong Kong in late autumn in 2022—Severe Tropical Storm Nalgae. Atmosphere, 14, 170.
4. Chan, P. W., Hon, K. K., & Foster, S. (2011). Wind data collected by a fixed-wing aircraft in the vicinity of a tropical cyclone over the south China coastal waters. Meteorologische Zeitschrift, 20, 313-321.
5. Chan, P. W., Wong, W. K., & Hon, K. K. (2014). Weather observations by aircraft reconnaissance inside Severe Typhoon Utor. Weather, 69, 199-203.
6. Chan, P. W., Wu, N. G., Zhang, C. Z., Deng, W. J., & Hon, K. K. (2018). The first complete dropsonde observation of a tropical cyclone over the South China Sea by the Hong Kong Observatory. Weather, 73, 227-234.

7. Chan, P.W., Zhang, Y., and Doviak, R.J. (2016). Calculation and application of eddy dissipation rate map based on spectrum width data of a S-band radar in Hong Kong. MAUSAM, 67, 411–422.
8. Deaves, D. M., & Harris, R. I. (1978). A Mathematical Model of the Structure of Strong Winds, CIRIA Report 76. London, the United Kingdom.
9. Drennan, W. M., Zhang, J. A., French, J. R., McCormick, C., & Black, P. G. (2007). Turbulent fluxes in the hurricane boundary layer. Part II: Latent heat flux. Journal of the Atmospheric Sciences, 64, 1103-1115.
10. Franklin, J. L., Black, M. L., & Valde, K. (2003). GPS dropwindsonde wind profiles in hurricanes and their operational implications. Weather and Forecasting, 18, 32-44.
11. French, J. R., Drennan, W. M., Zhang, J. A., & Black, P. G. (2007). Turbulent fluxes in the hurricane boundary layer. Part I: Momentum flux. Journal of the Atmospheric Sciences, 64, 1089-1102.
12. Giammanco, I. M., Schroeder, J. L., & Powell, M. D. (2013). GPS dropwindsonde and WSR-88D observations of tropical cyclone vertical wind profiles and their characteristics. Weather and Forecasting, 28, 77-99.
13. Gopalakrishnan, S., Hazelton, A., & Zhang, J. A. (2021). Improving hurricane boundary layer parameterization scheme based on observations. Earth and Space Science, e2020EA001422.
14. Gryning, S. E., Batchvarova, E., Brümmer, B., Jørgensen, H., & Larsen, S. (2007). On the extension of the wind profile over homogeneous terrain beyond the surface boundary layer. Boundary-Layer Meteorology, 124, 251-268.
15. He, J. Y., Hon, K. K., Chan, P. W., & Li, Q. S. (2022a). Dropsonde observations and numerical simulations for intensifying and weakening tropical cyclones over the northern part of the South China Sea. Weather, 77, 332-338.
16. He, J. Y., Hon, K. K., Li, Q. S., & Chan, P. W. (2022b). Wind profile analysis for selected tropical cyclones over the South China Sea based on dropsonde measurements. Atmósfera, 35, 111-126.
17. He, J. Y., Li, Q. S., Chan, P. W., Choy, C. W., Mak, B., Lam, C. C., & Luo, H. Y. (2023). An observational study of Typhoon Talim over the northern part of the South China Sea in July 2023. Atmosphere, 14, 1340.
18. Hock, T. F., & Franklin, J. L. (1999). The NCAR GPS dropwindsonde. Bulletin of the American Meteorological Society, 80, 407-420.
19. Hon, K. K., & Chan, P. W. (2022). A decade (2011–2020) of tropical cyclone reconnaissance flights over the South China Sea. Weather, 77, 308-314.
20. Kepert, J. D. (2006a). Observed boundary layer wind structure and balance in the hurricane core. Part I: Hurricane Georges. Journal of the Atmospheric Sciences, 63, 2169-2193.
21. Kepert, J. D. (2006b). Observed boundary layer wind structure and balance in the hurricane core. Part II: Hurricane Mitch. Journal of the Atmospheric Sciences, 63, 2194-2211.
22. Kwok, J., L. Chan, H.T. Yin, P.W. Li, and C.Y.Y. Leung, 2022: Automatic aviation turbulence detection using advanced machine learning techniques. Presented in Asia Oceania Geosciences Society (AOGS), 2022, 1-5 August 2022
23. Mellor, G. L., & Yamada, T. (1974). A hierarchy of turbulence closure models for planetary boundary layers. Journal of the Atmospheric Sciences, 31, 1791-1806.
24. Powell, M. D., Vickery, P. J., & Reinhold, T. A. (2003). Reduced drag coefficient for high wind speeds in tropical cyclones. Nature, 402, 279-283.
25. Sparks, N., Hon, K. K., Chan, P. W., Wang, S., Chan, J. C. L., Lee, T. C., & Toumi, R. (2019). Aircraft observations of tropical cyclone boundary layer turbulence over the South China Sea. Journal of the Atmospheric Sciences, 76, 3773-3783.
26. Sreenivasan, K. R. (1995). On the universality of the Kolmogorov constant. Physics of Fluids, 7, 2778-2784.
27. Stern, D. P., Bryan, G. H., & Aberson, S. D. (2016). Extreme low-level updrafts and wind speeds measured by dropsondes in tropical cyclones. Monthly Weather Review, 144, 2177-2204.
28. Stull, R. B. (1988). An Introduction to Boundary Layer Meteorology (1st ed.). Springer, Berlin, Germany.
29. Vecenaj, Z., Belusic, D., & Grisogono, B. (2010). Characteristics of the near-surface turbulence during a bora event. Annales Geophysicae, 28, 155-163.
30. Vickery, P. J., Wadhera, D., Powell, M. D., & Chen, Y. (2009). A hurricane boundary layer and wind field model for use in engineering applications. Journal of Applied Meteorology and Climatology, 48, 381-405.
31. Wang, J., Young, K., Hock, T., Lauritsen, D., Behringer, D., Black, M., Black, P. G., Franklin, J., Halverson, J., Molinari, J., Nguyen, L., Reale, T., Smith, J., Sun, B., Wang, Q., & Zhang, J. A. (2015). A long-term, high-quality, high-vertical-resolution GPS Dropsonde dataset for hurricane and other studies. Bulletin of the American Meteorological Society, 96, 961-973.
32. Wimmers, A., Griffin, S., Gerth, J., Bachmeier, S., & Lindstrom, S. (2018). Observations of gravity waves with high-pass filtering in the new generation of geostationary imagers and their relation to aircraft turbulence. Weather and Forecasting, 33(1), 139-144.
33. Zhang, J. A. (2010a). Estimation of dissipative heating using low-level in situ aircraft observations in the hurricane boundary layer. Journal of the Atmospheric Sciences, 67, 1853-1862.
34. Zhang, J. A. (2010b). Spectral characteristics of turbulence in the hurricane boundary layer over the ocean between the outer rain bands. Quarterly Journal of the Royal Meteorological Society, 136, 918-926.

35. Zhang, J. A., & Drennan, W. M. (2012). An observational study of vertical eddy diffusivity in the hurricane boundary layer. Journal of the Atmospheric Sciences, 69, 3223-3236.
36. Zhang, J. A., Marks, F. D., Montgomery, M. T., & Lorsolo, S. (2011). An estimation of turbulent characteristics in the low-level region of intense hurricanes Allen (1980) and Hugo (1989). Monthly Weather Review, 139, 1447-1462.
37. Zhang, J. A., & Montgomery, M. T. (2012). Observational estimates of the horizontal eddy diffusivity and mixing length in the low-level region of intense hurricanes. Journal of the Atmospheric Sciences, 69, 1306-1316.
38. Zhang, J. A., Rogers, R. F., Reasor, P. D., Uhlhorn, E. W., & Marks, F. D. (2013). Asymmetric hurricane boundary layer structure from dropsonde composites in relation to the environmental vertical wind shear. Monthly Weather Review, 141, 3968-3984.
39. Zhao, Z., Chan, P. W., Wu, N., Zhang, J. A., & Hon, K. K. (2019). Aircraft observations of turbulence characteristics in the tropical cyclone boundary layer. Boundary-Layer Meteorology, 174, 493-511.